

IOVS4NeRF: Incremental Optimal View Selection for Large-Scale NeRFs

Jingpeng Xie^{1,†}, Shiyu Tan^{1,†}, Yuanlei Wang¹, Tianle Du², Yifei Xue^{1,*}, Yizhen Lao^{1,*}

¹Hunan University, Changsha, China

²Nanchang University, Nanchang, China

Abstract—Large-scale Neural Radiance Fields (NeRF) reconstructions are typically hindered by the requirement for extensive image datasets and substantial computational resources. This paper introduces IOVS4NeRF, a framework that employs an uncertainty-guided incremental optimal view selection strategy adaptable to various NeRF implementations. Specifically, by leveraging a hybrid uncertainty model that combines rendering and positional uncertainties, the proposed method calculates the most informative view from among the candidates, thereby enabling incremental optimization of scene reconstruction. Our detailed experiments demonstrate that IOVS4NeRF achieves high-fidelity NeRF reconstruction with minimal computational resources, making it suitable for large-scale scene applications.

Index Terms—NeRF, Uncertainty Estimation, View Selection.

I. INTRODUCTION

Neural Radiance Fields (NeRF) [1] is an innovative method for synthesizing views by integrating 3D reconstruction with neural rendering. It uses implicit scene representation and differentiable volume rendering [2], requiring significant computational resources for large-scale scene reconstruction, often leading to inefficient processes [1]. Previous works [3, 4, 5, 6, 7] utilize combinations of hash functions, spherical harmonics, and both explicit and implicit scene representations to enable rapid training of NeRF. However, it still cannot cope with the challenge of large-scale scenes. Current efforts [8, 9, 10] have been made by decomposing large scenes into smaller segments, each trained by an isolated NeRF submodule, which necessitating substantial computational resources. In resource-limited settings, reconstructions exhibit severe artifacts and diminished visual fidelity in large scenes.

Drawing inspiration from the Next-Best View (NBV) problem [11], we expect each image in the limited input set to contain as much information as possible, thereby maximizing scene understanding and addressing the challenge of training large-scale NeRF under resource constraints. Emerging studies [12, 13, 14] use uncertainty-guided NBV selection, but they often modify the internal network, which can affect reusability. Other approaches [15, 16] make no changes to NeRF architecture but focus primarily on pixel-level uncertainty during

This work is supported by the National Key R&D Program of China (Grant NO. 2022ZD0119000), Hunan Provincial Key R&D Program of China (Grant NO. 2024JK2020 and 024JK2021), Hunan Provincial Natural Science Foundation of China (Grant NO. 2024JJ10027), Young Talents of Huxiang (Grant NO. Z20243300575), Lushan Lab Research Funding, and Changsha Science Fund for Distinguished Young Scholars (Grant NO. kq2306002).

† Equal contribution. * Corresponding authors.

rendering. While these methods have shown promise, they still face issues with artifacts and efficiency when applied to large-scale scenes.

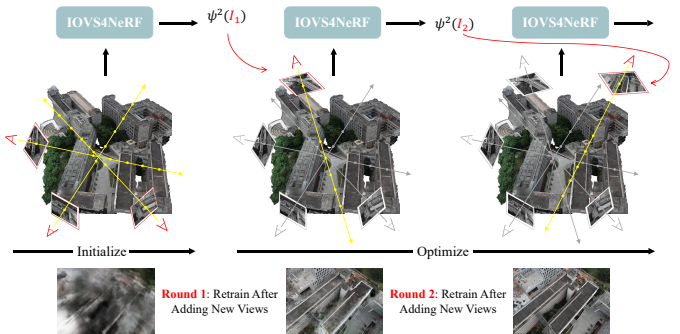


Fig. 1: **IOVS4NeRF** is a flexible framework that actively expands the existing training set with newly captured samples based on hybrid uncertainties of candidate views.

Building on the above background, we model the emission radiation values of each position in the scene as a Gaussian distribution rather than a single value. This approach prevents NeRF from collapsing into trivial solutions with incomplete scene observations. Inspired by oblique photography [17], we incorporate both planar and non-planar UAV flight paths [18, 19] to assess positional uncertainty. We combine these uncertainties into a hybrid metric to optimize view selection, as illustrated in Fig. 1.

Furthermore, we accelerate the reconstruction speed by employing a lightweight NeRF from the perspective of the model structure. In this paper, we use Instant-NGP [3] because its multi-resolution hash encoding has adaptive and efficient characteristics, making it well-adaptable to scenes of different scales. In summary, our contributions are as follows:

- We propose a NeRF-based framework for incremental optimal view selection to address the limitations of NeRFs in large-scale scenes with restrained computational cost.
- We define a novel estimation of uncertainty, consisting of rendering and positional uncertainty, to compute the information gain of each candidate view.
- We evaluate our method on real-world datasets, showing it significantly reduces time while maintaining reconstruction effectiveness compared to previous baselines.

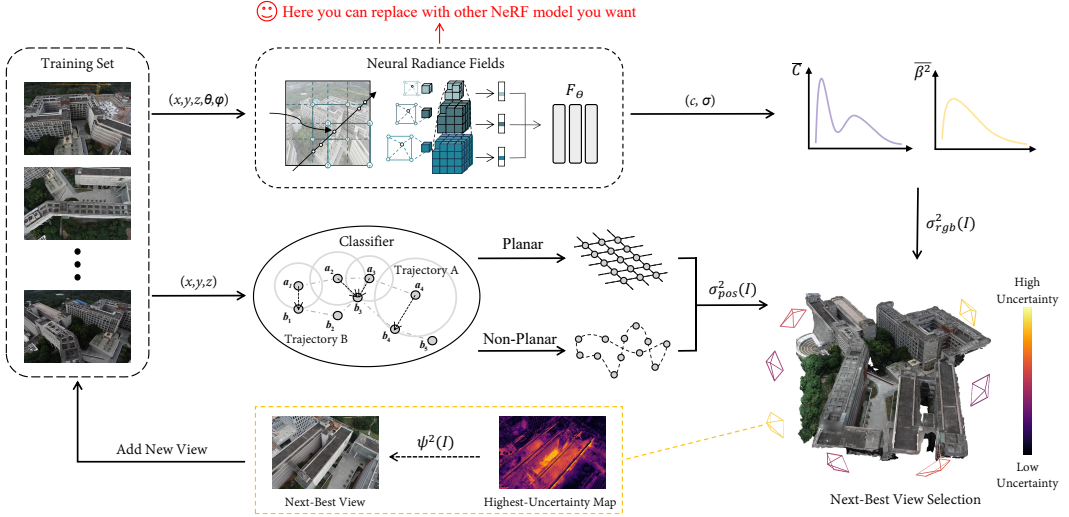


Fig. 2: **Overview of Our Framework.** It consists of three parts: I. We train NeRF using 5D image information, modeling color as a Gaussian distribution to compute rendering uncertainty. II. We calculate positional uncertainty from training images using a classifier, combining it with rendering uncertainty to form hybrid uncertainty. III. The image with the highest hybrid uncertainty is iteratively added to the training set until the desired reconstruction quality or image limit is reached.

II. METHODOLOGY

As illustrated in Fig. 2, our proposed IOVS4NeRF introduces, in epistemic uncertainty mind [20], a hybrid uncertainty, which can be reduced by collecting more data.

IOVS4NeRF selects the best view using a *hybrid uncertainty* that combines rendering and positional uncertainty. For rendering uncertainty, 5D coordinates (\mathbf{x}, \mathbf{d}) are input into a NeRF network, which outputs color c and volume density σ . These are used to calculate image uncertainty as a Gaussian distribution. Positional uncertainty is derived using 3D coordinates x , with a classifier determining trajectory type and Voronoi diagrams estimating information. These two uncertainties are normalized and summed to form the hybrid uncertainty:

$$\psi^2(I) = \text{Norm}(\sigma_{pos}^2(I)) + \text{Norm}(\sigma_{rgb}^2(I)), \quad (1)$$

where I is the ground truth image, and $\sigma_{rgb}^2(I)$ and $\sigma_{pos}^2(I)$ are rendering and positional uncertainty respectively.

A. Rendering Uncertainty

NeRF [1] represents a scene as a continuous function F_θ that outputs both the emitted radiance value and volume density. Specifically, given a 3D $\mathbf{x} = (x, y, z)$ and a viewing direction vector $\mathbf{d} = (\theta, \phi)$, a multi-layer perceptron model is used to generate the corresponding color c and volume density σ .

NeRF utilizes volume rendering to determine the color of rays passing through the scene, enabling novel view synthesis. Given a camera ray $\mathbf{r}(t) = \mathbf{o} + t\mathbf{d}$ with the camera center $\mathbf{o} \in \mathbb{R}^3$ passing through a specific pixel on the image plane, the color of the pixel is calculated by volume rendering integration, approximating integrals via stratified sampling discrete points can be expressed as:

$$\hat{C}(\mathbf{r}) = \sum_{i=1}^{N_s} \alpha_i c(\mathbf{r}(t_i)), \quad (2)$$

$$\alpha_i = \exp \left(- \sum_{j=1}^{i-1} \sigma_j \delta_j \right) (1 - \exp(-\sigma_i \delta_i)), \quad (3)$$

where $\delta_i = t_{i+1} - t_i$ is the distance between samples, and N_s denotes the number of samples.

To improve results with limited training data, we model RGB values as Gaussian distributions[14], using variance to represent uncertainty. We add a variance branch to NeRF's MLP, defining variance via information entropy:

$$\beta^2(\mathbf{r}(t_i)) = -P(\alpha_i) \log P(\alpha_i), \quad (4)$$

where α_i is the same as Eq. (2), and $P(\cdot)$ represents proportion of α_i in the $\sum \alpha_i$ along the ray.

Given the conjugacy of Gaussian distributions, the rendered values along a ray also follow a Gaussian distribution:

$$\hat{C}(\mathbf{r}) \sim \text{Beta}(\bar{C}(\mathbf{r}), \bar{\beta}^2(\mathbf{r})), \quad (5)$$

where

$$\bar{C}(\mathbf{r}) = \sum_{i=1}^{N_s} \alpha_i c(\mathbf{r}(t_i)), \quad \bar{\beta}^2(\mathbf{r}) = \sum_{i=1}^{N_s} \alpha_i^2 \beta^2(\mathbf{r}(t_i)) \quad (6)$$

Assuming ray independence, rendering uncertainty is maximized by the log-likelihood of rays from the same image:

$$\sigma_{rgb}^2(I) = \sum_{i=1}^{N_r} \frac{\|C(\mathbf{r}_i) - \bar{C}(\mathbf{r}_i)\|_2^2}{2\bar{\beta}^2(\mathbf{r}_i)} + \frac{\log \bar{\beta}^2(\mathbf{r}_i)}{2}, \quad (7)$$

where N_r means the total number of the rays in photo I .

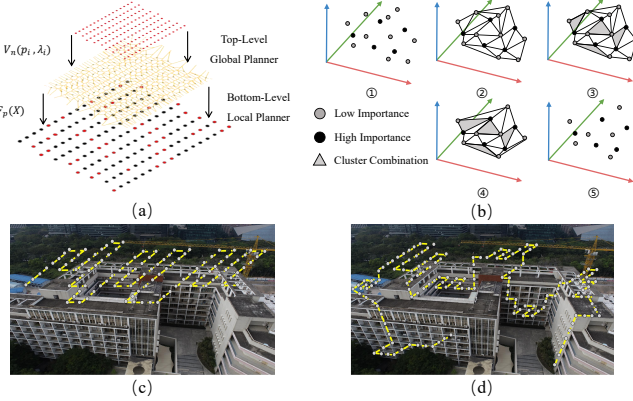


Fig. 3: (a) We use a Voronoi-based method, where a top-level planner updates nodes and a bottom-level planner refines them based on potential fields. (b) We cluster points based on maximum volume and local density, quantifying uncertainty through importance values and density measures. (c) Planar flight trajectory. (d) Non-planar flight trajectory.

B. Positional Uncertainty

It has been determined that most UAV flight paths that can be programmed follow an approximate planar trajectory[17], but users can freely manipulate the UAV to fly along non-planar trajectories. Therefore, we design a classifier to determine whether a UAV flight trajectory is planar or non-planar. To implement this adaptive classifier, we divide the data points into two groups, $A = \{a_1, \dots, a_p\}$ and $B = \{b_1, \dots, b_q\}$, and measure their similarity using the Hausdorff distance[21]. The Hausdorff distance offers a direct measure of trajectory similarity, bypassing interpolation and reducing noise. We set a threshold and classify trajectories as non-planar if their distance exceeds this threshold.

For planar trajectories, we use a Voronoi-based information gain radiance field[22] within a hierarchical planning framework. The top-level global planner creates a collision-free graph using an improved Voronoi diagram. It traverses nodes to cover maximum uncertainty, while the bottom-level local planner refines this by selecting the most significant node based on weighted centroids. Specifically, we compress 3D pose information points to two-dimensional Euclidean space and define p_i as n distinct points on this space, and λ_i as the weighted value of a given point. Then, $V_n(p_i, \lambda_i)$ is the V-region of point p_i with weight λ_i , where $d(p, p_i)$ is the Euclidean distance between p and p_i :

$$V_n(p_i, \lambda_i) = \bigcap_{j \neq i} \left\{ p \mid \frac{d(p, p_i)}{\lambda_i} < \frac{d(p, p_j)}{\lambda_j} \right\} \quad (8)$$

In a non-confusing context, we abbreviate $V_n(p_i, \lambda_i)$ as $V_n(p_i)$. Based on this, the uncertainty of our plane's Voronoi regions is defined as:

$$F_p(I) = \sum_{i=1}^{N_v} \frac{\sum_{j=1}^{N_v} \|p_i - p_j\|^\lambda_i}{A_i}, \quad (9)$$

where A_i represents area of the Voronoi polygon $V_n(p_i)$, and N_v means the total number of 3D pose points.

We use the Voronoi clustering algorithm[23] to cluster points based on a volume threshold for non-planar trajectories. Point cluster generalization translates large-scale information into smaller diagrams, considering topological and metric factors. We combine importance values and local density to evaluate changes in importance across areas. The larger the area of the Voronoi polygon, the greater the weight. Thus, points are more likely to be retained in generalized mapping. The importance value equation is as follows:

$$G_i = \frac{\lambda_i A_i}{\sum_{k=1}^{N_v} (\lambda_k A_k)}, \quad (10)$$

where G_i is the probability of selecting the specific point and given by the product of the area of the Voronoi polygon, denoted as A_i , and the weight value, denoted as λ_i .

Relative local density enables the comparison of density changes point by point before and after generalization, thus better assessing the density changes between points before and after generalization. As follows:

$$r_i = \frac{\frac{1}{A_i}}{\sum_{k=1}^{N_v} \frac{1}{A_k}} \quad (11)$$

The positional uncertainty of non-planer trajectory is:

$$F_{np}(I) = \sum_{i=1}^{N_v} -\log(G_i)r_i + \lambda_i \|G_i - r_i\|^2 \quad (12)$$

Therefore, the total positional uncertainty is:

$$\sigma_{pos}^2(I) = \mathbb{I}(p)F_p(I) + \mathbb{I}(np)F_{np}(I), \quad (13)$$

where $\mathbb{I}(\cdot)$ is the indicator function.

III. EXPERIMENTS

A. Experimental Setup

The six sets of UAV data we use come from four large-scale datasets: two benchmarks from Mill-19, two from Urban-3D, one from Pix-4D, and one self-captured footage dataset from Changsha, Hunan. Due to GPU limitations, we randomly select 500 images for each dataset as the whole image set (if the total number of images in a dataset is less than 500, we use all the images instead). We randomly choose 15% of the images in each dataset for initialization and randomly select 10% of the images as the test set. Then, we incrementally select 15% of the images using various view selection methods as the optimal views for incremental training. Thus, only 30% of the full image set is used to train.

We input the ground truth RGB images into COLMAP, which is a software to recover the structures from images to get the pose of each image and utilize the Instant-NGP[3] to demonstrate the effectiveness of the proposed IOVS4NeRF. All the experiments are conducted with an Intel core i9 CPU and an NVIDIA GeForce 3090 GPU (24GB memory).

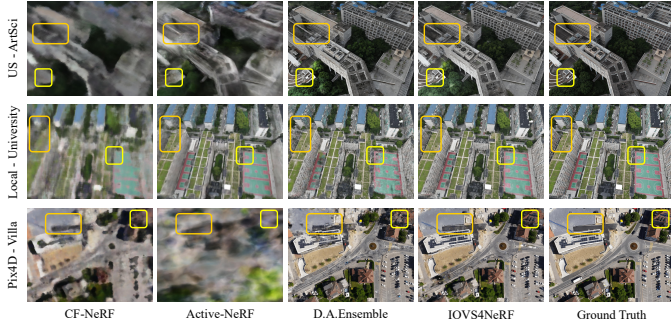


Fig. 4: Rendering effect visualization of different methods (partial experimental results).

B. Comparison Experiment

To evaluate the results and computational costs of methods applied to large-scale scene reconstruction of UAV, we will compare IOVS4NeRF with three current popular methods[13, 14, 15] designed to exclusively estimate uncertainty in NeRF-based models. Additionally, evaluation metrics are considered from both image quality and uncertainty.

TABLE I: Quantitative results of different methods in comparison experiment (best shown in **green** and second in **blue**).

Scenes	Methods	Quality			Uncertainty		Time \downarrow
		PSNR \uparrow	SSIM \uparrow	LPIPS \downarrow	AUSE \downarrow	SRCC \uparrow	
Building	CF-NeRF	14.926	0.260	0.738	0.100	0.706	12:57
	Active-NeRF	12.430	0.231	0.777	0.141	0.464	17:45
	D.A. Ensemble	16.857	0.383	0.422	0.303	0.668	12:18
	IOVS4NeRF	19.841	0.469	0.351	0.055	0.878	7:28
Rubble	CF-NeRF	17.758	0.312	0.717	0.075	0.815	12:58
	Active-NeRF	16.531	0.275	0.622	0.097	0.683	17:47
	D.A. Ensemble	19.629	0.507	0.335	0.257	0.818	12:20
	IOVS4NeRF	21.108	0.573	0.303	0.052	0.884	7:29
Polytech	CF-NeRF	14.259	0.251	0.731	0.118	0.751	12:57
	Active-NeRF	8.888	0.153	0.747	0.264	-0.035	17:46
	D.A. Ensemble	20.673	0.564	0.253	0.058	0.915	12:46
	IOVS4NeRF	21.810	0.592	0.235	0.053	0.925	7:48
ArtSci	CF-NeRF	15.578	0.227	0.693	0.106	0.729	12:57
	Active-NeRF	13.531	0.193	0.610	0.152	0.525	17:48
	D.A. Ensemble	17.769	0.463	0.338	0.101	0.793	13:28
	IOVS4NeRF	18.836	0.500	0.319	0.083	0.834	8:21
University	CF-NeRF	15.359	0.189	0.669	0.112	0.645	12:58
	Active-NeRF	17.814	0.359	0.359	0.087	0.780	17:46
	D.A. Ensemble	16.610	0.331	0.416	0.101	0.682	12:08
	IOVS4NeRF	18.722	0.430	0.327	0.077	0.814	6:47
Villa	CF-NeRF	15.141	0.259	0.645	0.111	0.777	12:58
	Active-NeRF	9.236	0.121	0.828	0.242	0.055	20:32
	D.A. Ensemble	15.415	0.337	0.494	0.123	0.689	13:58
	IOVS4NeRF	18.250	0.457	0.386	0.079	0.868	8:46

This comparison experiment demonstrates that our uncertainty estimation strongly correlates with novel view synthesis quality for NeRFs. As shown in Fig. 4 and Table. I, IOVS4NeRF achieves significantly more information in uncertainty prediction with respect to synthesis error. The superior performance of our approach demonstrates the proposed hybrid uncertainty leads to more consistent uncertainty estimates.

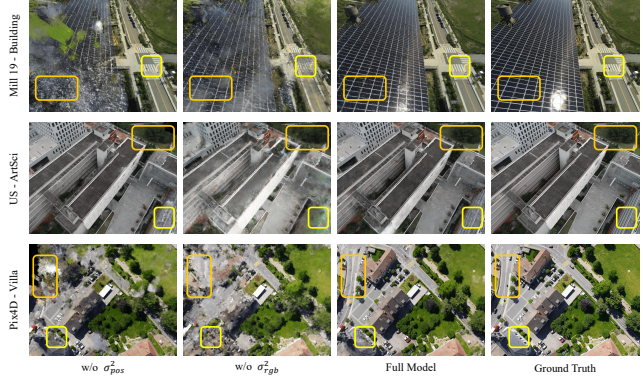


Fig. 5: Rendering effect visualization of different components (partial experimental results).

TABLE II: Quantitative results of different components in ablation study(best shown in **green** and second in **blue**).

Component \ Scene	Building	Rubble	Polytech	ArtSci	Villa	University
w/o σ_{pos}^2	PSNR \uparrow	17.031	19.803	19.856	18.386	15.937
	SSIM \uparrow	0.404	0.527	0.541	0.497	0.356
	LPIPS \downarrow	0.407	0.645	0.731	0.693	0.645
w/o σ_{rgb}^2	PSNR \uparrow	17.841	20.045	18.606	17.687	15.917
	SSIM \uparrow	0.390	0.491	0.534	0.451	0.368
	LPIPS \downarrow	0.421	0.341	0.534	0.352	0.475
Full Model	PSNR \uparrow	19.841	21.108	21.810	18.836	18.250
	SSIM \uparrow	0.469	0.573	0.592	0.500	0.457
	LPIPS \downarrow	0.351	0.303	0.235	0.319	0.386

C. Ablation Study

The ablation study aims to assess the impact of the individual components within our hybrid uncertainty model. The result, as depicted in Fig. 5 and Table. II, demonstrates that omitting the positional uncertainty component, σ_{pos}^2 , leads to high-fidelity rendering in localized areas. However, this setting neglects broader scene coverage, as the next view selection is biased towards the unrendered regions. Conversely, disregarding the rendering uncertainty component, σ_{rgb}^2 , results in a globally low-fidelity rendering. This occurs due to the next view selection overextending its reach, attempting to encompass the entire spatial extent. In contrast, our proposed hybrid uncertainty consistently produces superior outcomes by employing the combined measure of σ_{rgb}^2 and σ_{pos}^2 . This indicates the synergistic benefits of incorporating both components into the uncertainty estimation process.

CONCLUSION

In this paper, we propose an incremental optimal view selection framework, IOVS4NeRF, aiming at addressing the limitations of NeRF in resource-constrained scenarios. By expanding the training dataset with strategically selected samples based on a novel hybrid uncertainty, which takes into account both rendering uncertainty and positional uncertainty of different flight trajectories, IOVS4NeRF significantly enhances the quality of novel view synthesis while minimizing additional resource requirements. The efficacy has been validated through extensive experiments on large-scale realistic scenes, demonstrating its robustness even with limited training data. In future work, our proposed method could be extended to accommodate a broader range of scale-varying scenarios.

REFERENCES

[1] B. Mildenhall, P. P. Srinivasan, M. Tancik, J. T. Barron, R. Ramamoorthi, and R. Ng, “Nerf: Representing scenes as neural radiance fields for view synthesis,” *Communications of the ACM*, vol. 65, no. 1, pp. 99–106, 2021.

[2] A. Yu, V. Ye, M. Tancik, and A. Kanazawa, “pixelnerf: Neural radiance fields from one or few images,” in *Proceedings of the IEEE/CVF conference on computer vision and pattern recognition*, 2021, pp. 4578–4587.

[3] T. Müller, A. Evans, C. Schied, and A. Keller, “Instant neural graphics primitives with a multiresolution hash encoding,” *ACM transactions on graphics (TOG)*, vol. 41, no. 4, pp. 1–15, 2022.

[4] A. Chen, Z. Xu, A. Geiger, J. Yu, and H. Su, “Tensorf: Tensorial radiance fields,” in *European conference on computer vision*. Springer, 2022, pp. 333–350.

[5] S. Fridovich-Keil, A. Yu, M. Tancik, Q. Chen, B. Recht, and A. Kanazawa, “Plenoxels: Radiance fields without neural networks,” in *Proceedings of the IEEE/CVF conference on computer vision and pattern recognition*, 2022, pp. 5501–5510.

[6] C. Sun, M. Sun, and H.-T. Chen, “Direct voxel grid optimization: Super-fast convergence for radiance fields reconstruction,” in *Proceedings of the IEEE/CVF conference on computer vision and pattern recognition*, 2022, pp. 5459–5469.

[7] Q. Xu, Z. Xu, J. Philip, S. Bi, Z. Shu, K. Sunkavalli, and U. Neumann, “Point-nerf: Point-based neural radiance fields,” in *Proceedings of the IEEE/CVF conference on computer vision and pattern recognition*, 2022, pp. 5438–5448.

[8] H. Turki, D. Ramanan, and M. Satyanarayanan, “Megnerf: Scalable construction of large-scale nerfs for virtual fly-throughs,” in *Proceedings of the IEEE/CVF Conference on Computer Vision and Pattern Recognition*, 2022, pp. 12922–12931.

[9] M. Tancik, V. Casser, X. Yan, S. Pradhan, B. Mildenhall, P. P. Srinivasan, J. T. Barron, and H. Kretzschmar, “Block-nerf: Scalable large scene neural view synthesis,” in *Proceedings of the IEEE/CVF Conference on Computer Vision and Pattern Recognition*, 2022, pp. 8248–8258.

[10] M. Zhenxing and D. Xu, “Switch-nerf: Learning scene decomposition with mixture of experts for large-scale neural radiance fields,” in *The Eleventh International Conference on Learning Representations*, 2022.

[11] R. Zeng, Y. Wen, W. Zhao, and Y.-J. Liu, “View planning in robot active vision: A survey of systems, algorithms, and applications,” *Computational Visual Media*, vol. 6, pp. 225–245, 2020.

[12] J. Shen, A. Ruiz, A. Agudo, and F. Moreno-Noguer, “Stochastic neural radiance fields: Quantifying uncertainty in implicit 3d representations,” in *2021 International Conference on 3D Vision (3DV)*. IEEE, 2021, pp. 972–981.

[13] J. Shen, A. Agudo, F. Moreno-Noguer, and A. Ruiz, “Conditional-flow nerf: Accurate 3d modelling with reliable uncertainty quantification,” in *European Conference on Computer Vision*. Springer, 2022, pp. 540–557.

[14] X. Pan, Z. Lai, S. Song, and G. Huang, “Activenerf: Learning where to see with uncertainty estimation,” in *European Conference on Computer Vision*. Springer, 2022, pp. 230–246.

[15] N. Sünderhauf, J. Abou-Chakra, and D. Miller, “Density-aware nerf ensembles: Quantifying predictive uncertainty in neural radiance fields,” in *2023 IEEE International Conference on Robotics and Automation (ICRA)*. IEEE, 2023, pp. 9370–9376.

[16] S. Lee, L. Chen, J. Wang, A. Liniger, S. Kumar, and F. Yu, “Uncertainty guided policy for active robotic 3d reconstruction using neural radiance fields,” *IEEE Robotics and Automation Letters*, vol. 7, no. 4, pp. 12070–12077, 2022.

[17] T. Zhou, L. Lv, J. Liu, and J. Wan, “Application of uav oblique photography in real scene 3d modeling,” *The International Archives of the Photogrammetry, Remote Sensing and Spatial Information Sciences*, vol. 43, pp. 413–418, 2021.

[18] M. Roberts, D. Dey, A. Truong, S. Sinha, S. Shah, A. Kapoor, P. Hanrahan, and N. Joshi, “Submodular trajectory optimization for aerial 3d scanning,” in *Proceedings of the IEEE International Conference on Computer Vision*, 2017, pp. 5324–5333.

[19] G. Petrie, “Systematic oblique aerial photography using multiple digital frame camera,” *Photogrammetric Engineering & Remote Sensing*, pp. 102–107, 2009.

[20] A. Kendall and Y. Gal, “What uncertainties do we need in bayesian deep learning for computer vision?” *Advances in neural information processing systems*, vol. 30, 2017.

[21] M.-P. Dubuisson and A. K. Jain, “A modified hausdorff distance for object matching,” in *Proceedings of 12th international conference on pattern recognition*, vol. 1. IEEE, 1994, pp. 566–568.

[22] K. Ok, S. Ansari, B. Gallagher, W. Sica, F. Dellaert, and M. Stilman, “Path planning with uncertainty: Voronoi uncertainty fields,” in *2013 IEEE International Conference on Robotics and Automation*. IEEE, 2013, pp. 4596–4601.

[23] H. Yan and R. Weibel, “An algorithm for point cluster generalization based on the voronoi diagram,” *Computers & Geosciences*, vol. 34, no. 8, pp. 939–954, 2008.